Processing and properties of novel ZnO−Bi$_2$O$_3$−B$_2$O$_3$ glass-ceramic nanocomposites

Casey M. Schwarz [a, *], Myungkoo Kang [b], Quentin Altemose [a], Katrina Raichle [a], Brittani Schnable [a], Christopher Grabill [d], Jarrett Rice [e], Mia Truman [a], Carlo Pantano [e], Ilya Mingareev [b, c], Laura Sisken [b], Clara Rivero-Baleine [f], Kathleen A. Richardson [b], Stephen M. Kuebler [b, d, g]

[a] Physics & Astronomy Department, Ursinus College, Collegeville, PA, 19426, USA
[b] CREOL, The College of Optics and Photonics, University of Central Florida, Orlando, FL, 32816, USA
[c] Mechanical and Civil Engineering, Florida Institute of Technology, Melbourne, FL, 32901, USA
[d] Chemistry Department, University of Central Florida, Orlando, FL, 32816, USA
[e] Department of Materials Science and Engineering, Pennsylvania State University, University Park, PA, 16802, USA
[f] Lockheed Martin, Orlando, FL, 32819, USA
[g] Physics Department, University of Central Florida, Orlando, FL, 32816, USA

ARTICLE INFO

ABSTRACT

Transparent optical glass-ceramics consisting of nanocrystals have the potential for use as optical devices such as waveguides, microlenses, and photonic crystals. ZnO−Bi$_2$O$_3$−B$_2$O$_3$ based glass ceramics were prepared via a melt quenching technique to assess parent glass and post-processed property evolution. Here, three large scale melts and six small test melts of the glass were melted at and around the 33.3 ZnO-33.3 Bi$_2$O$_3$- 33.3 B$_2$O$_3$ molar composition; some were also doped with small quantities of As$_2$O$_3$ for redox control or with LiNO$_3$ as a nucleating agent. The physical and chemical properties including thermal behavior, transmission, elemental, and index of refraction of these melts were compared to assess their suitability as optical glasses and glass ceramics. Heat treatments were used to create transparent ZnO−Bi$_2$O$_3$−B$_2$O$_3$ glass ceramics containing BiB$_3$O$_6$ and Bi$_2$ZnB$_2$O$_7$ nanocrystals. We correlate nucleation temperature, heat treatment temperature, and heat treatment duration with induced crystal phase formation. In addition to BiB$_3$O$_6$ and Bi$_2$ZnB$_2$O$_7$ nanocrystals, ZnO was found to grow on the surface of some compositions. Compositional optimization and heat treatment procedures were developed to encourage volume crystallization while mitigating unwanted surface crystal growth. Laser-induced crystallization pads and lines were patterned in the glass to compare with and assess post-heat treatment phase and structure modification.

© 2019 Elsevier B.V. All rights reserved.

1. Introduction

Transparent glass-ceramics containing nanocrystals with unique optical functionality have generated increased interest for their promising role in photonics, optics, laser science and technology [1–3]. Glass compositions based on the binary bismuth borate systems (BiB$_3$O$_6$ and BiBO$_3$) have been studied for their attractive properties such as their high laser damage threshold, wide transparency across the UV−visible regions, high density and

refractive index [4−6]. More recently, this glass system and the composites based upon its possible conversion to glass ceramics, have gained interest for their optical nonlinearities [1,7]. The zinc bismuth borate glass system (ZnO−Bi$_2$O$_3$−B$_2$O$_3$) has also been studied for its interesting nonlinear properties along with the ability to produce Bi$_2$ZnB$_2$O$_7$ nanocrystals throughout its matrix. The Bi$_2$ZnB$_2$O$_7$ crystal is reported to have a large second-harmonic generation (SHG) response and is a promising nonlinear optical material [1]. These nanocrystals along with other phases can be precipitated via heat treatments or laser exposures. In the ZnO−Bi$_2$O$_3$−B$_2$O$_3$ system, heat treatments were used to precipitate BiB$_3$O$_6$ and Bi$_2$ZnB$_2$O$_7$ nanocrystals [1,3,8,9]. Bi$_2$ZnB$_2$O$_7$ nanocrystals were also produced by femtosecond laser exposures [2]. In

the 3Sm₂O₃-30.3Bi₂O₃-33.3ZnO-33.3B₂O₃ system, nanocrystal Bi₂ZnB₂O₇ lines were formed within the glass by laser writing [10]. $ZnO-Bi_2O_3-B_2O_3$ glasses containing $Bi_2ZnB_2O_7$ nanocrystals have great potential for the microfabrication of photonic devices such as waveguide components and optical gratings [1,3,10].

The inherent complexity of the nanocrystal growth process is still an obstacle for realizing many of the potential applications and microdevices [2]. The ability to produce nanocrystals in a homogenous optically transparent matrix along with the ability to control the crystal's spatial location (surface or volume), size, and number density using a combination of heat treatments and laser exposures would be highly desirable for a wealth of optical device applications. Additionally, the use of subsequent heat treatments along with laser exposure for crystal nucleation and growth has yet to be exploited.

To better understand the $Bi_2ZnB_2O_7$ nanocrystal growth process in the $ZnO-Bi_2O_3-B_2O_3$ matrix we have systematically studied various $ZnO-Bi_2O_3-B_2O_3$ compositions and their resulting physical, optical, and thermal properties. We have quantified how these properties change under heat treatment and/or laser processing. Three large scale melts and six small test melts of the glass were melted at and around the 33.3 ZnO-33.3 Bi₂O₃- 33.3 B₂O₃ molar composition, including some that were also doped with small quantities of As₂O₃ for redox control or with LiNO₃ as a nucleating agent were explored. Through analysis of pre- and post-treatment samples we have correlated nucleation temperature, heat treatment temperature, and heat treatment duration with induced crystal phase formation and growth. $ZnO-Bi_2O_3-B_2O_3$ materials which exhibited nanocrystal formation without loss of transmission were selected for further experiments and laser exposure. Under heat treatments and laser exposure the $ZnO-Bi_2O_3-B_2O_3$ glass including As₂O₃ resulted in precipitated $Bi_2ZnB_2O_7$ nanocrystals within the matrix volume. This optimization and control is useful for the development of optical devices with tunable properties.

2. Experimental

2.1. Glass melting

Glass samples were prepared using a standard melt quenching technique [1,11]. The mixture of compositions were created using varying molar amounts of ZnO, Bi₂O₃ and B₂O₃, some of which included excess B₂O₃ and LiNO₃. The small melt batches were prepared using Bi₂O₃, ZnO, and B₂O₃ starting materials, with some having added LiNO₃ or As₂O₃ content. The large melts were prepared at SCHOTT North America, Inc. Each batch was melted in a platinum/platinum-rhodium crucible for approximately 1–1.5 h at a temperature of 900 °C or 1000 °C (Table 1). The melts were poured onto a stainless steel mold and annealed for various temperatures and durations. Individual samples of sizes approximately 10.0 mm × 10.0 mm × 2.0 mm were cut from the melts and optically polished. These samples were then used for characterization.

2.2. Goals for the various melt compositions

Multiple glasses were prepared and the compositions were chosen to evaluate specific variables believed to impact crystal formation. The composition 33.33ZnO-33.33Bi₂O₃-33.34B₂O₃ is stoichiometric with the targeted ZnBi₂B₂O₇ crystal phase. The composition $30ZnO-30Bi_2O_3-40B_2O_3$ contains excess B₂O₃ relative to the crystal composition; it was fabricated to evaluate the effects of excess glass former in a melt exhibiting a slight decrease in viscosity. The composition $30ZnO-40Bi_2O_3-30B_2O_3$ contains excess Bi₂O₃ (~5 mol %) relative to the crystal composition;

considering the volatility and redox sensitivity of Bi-oxide, it was fabricated to explore any possible effects of Bi content. The composition $40ZnO-30Bi_2O_3-30B_2O_3$ is the composition reported by Zheng et al., and it contains excess ZnO (~5 mol %) relative to the crystal composition [1]. The composition 31.66ZnO-31.66Bi₂O₃-31.67B₂O₃–5LiNO₃ maintains the stoichiometric ratios between the Zn, Bi and B but adds ~5% LiNO₃ which adds a typical nucleating species (Li) and excess oxygen to maintain the Bi5+ oxidation state. The composition 31.6ZnO-31.6Bi₂O₃-31.6B₂O₃-5.2As₂O₃ also maintains the stoichiometric ratios between the Zn, Bi and B but adds ~5% As₂O₃ to maintain the Bi5+ oxidation state.

2.3. Glass sample characterization

Thermal analysis was employed to assess glass transition (T_g), crystallization (T_x, T_p) and melting (T_m) temperatures. Measurements for all melts were made using a differential scanning calorimeter (DSC) (TA Instruments DSC 2920 and SDT 2960) in a nitrogen atmosphere. Measurements were made using a heating rate of 10 °C per minute and heating range from room temperature up to 600–700 °C. Glass transition temperatures T_g were determined from the DSC curves using the intersection of tangents from the baseline and initial slope of the step. Crystallization temperatures were determined from the DSC curves using the onset positions (T_x) and peak positions (T_p) of the exothermic peaks. Melting temperatures T_m were determined from the DSC curves using the peak positions of the endothermic peaks. Raman spectroscopy (Bruker Senterra) was used to identify molecular connectivity within the glass matrix, with an excitation wavelength is 785 nm, a resolution of 3–5 cm⁻¹, a power of 1 mW, and a 10x objective. Refractive index measurements were made using a modified IR Metricon (model 2010) at a wavelength of 1880 nm. To modify the system for IR measurements, a GaP prism was used and an optical parametric oscillator (OPO) laser, manufactured by M² Lasers (Firefly-IR) served as the IR source. The OPOs offer tunable wavelength selection in the ranging from approximately 1500 nm–4800 nm. The OPO is a pulsed laser that operated at a repetition rate of 112 kHz. This glass samples are transparent in the visible, up to 3 μm. The choice of 1880 nm for index measurements is a standard line used based off of dispersion curve transmission. The coefficients of transmission for all samples ranged from 0.78 to 0.80. A scanning electron microscope (SEM) (Zeiss ULTRA-55 FEG SEM) equipped with an energy-dispersive X-Ray spectroscopy (EDS) tool was used for surface and elemental analysis. It is known that obtaining an accurate measurement for lighter elements, specifically boron in our case, is challenging using the EDS tool. Therefore, X-Ray fluorescence spectroscopy (XRF) was used in combination with EDS for elemental analysis. VIS/NIR transmission and reflection spectroscopy (Jasco) with a wavelength measurement range of 200 nm to 3 μm was used to measure the optical bandgap and IR transmissivity. FTIR transmission spectroscopy (Thermo Scientific, Nicolet iS5) was used to assess the same at wavelengths beyond the Jasco system. X-ray diffraction (XRD) (PANalytical Empyrean) was used to determine crystal phase over 2θ range of 10° to 80°. Transmission Electron Microscopy (TEM) (FEI Tecnai F30 TEM) combined with Selected Area Electron Diffraction (SAED) was used to determine for size, density, and identification of nanometer sized secondary phases.

2.4. Heat treatments

Heat treatments on glass specimens were conducted by placing the bulk or powdered sample in either a furnace or via placement within an *in-situ* XRD temperature and atmosphere controlled chamber. The atmosphere was air unless otherwise noted. Heat

Table 1
Glass composition and preparation conditions of ZnO−Bi$_2$O$_3$−B$_2$O$_3$ based glasses.

Glass Sample	Composition (mol%) as batched and (confirmed via EDS)	Melt size/crucible	Melt atm.	Melt and anneal time and temperature
LM1-40/30/30	40ZnO-30 Bi$_2$O$_3$−30B$_2$O$_3$ (EDS: 38.1ZnO-31.1Bi$_2$O$_3$-30.8B$_2$O$_3$)	500 g/platinum	AIR	1000 °C/1hr + additional 1000 °C for 1.5hr. Glass was cast at 900 °C and annealed at 400 °C for 1hr. Cooled to rm temp at 30 °C/h.
LM2-40/30/30	40ZnO−30Bi$_2$O$_3$−30B$_2$O$_3$ (Cast 1) (EDS: 39.2ZnO-30.4Bi$_2$O$_3$-30.4B$_2$O$_3$) 40ZnO−30Bi$_2$O$_3$−30B$_2$O$_3$ (Cast 2)	2000 g/platinum	AIR	1000 °C/1.5hr + additional 1000 °C for 1.5hr. Glass was cast at 850 °C (Cast 1) and 775 °C (Cast 2) and annealed at 410 °C for 1hr. Cooled to rm temp at 30 °C/h.
LM3-40/30/30 + As	40ZnO−30Bi$_2$O$_3$−30B$_2$O$_3$ (0.5 wt % As$_2$O$_3$)	500 g, Pt pot with Pt bubbler tube and stirrer	O$_2$ cover gas	Melted at 900 °C/1hr and cast at 800 °C. Annealed at 400 °C/1hr. Cooled to rm temp at 40 °C/h.
SM1-33/33/33	33.33ZnO-33.33Bi$_2$O$_3$-33.34B$_2$O$_3$	180 g/platinum rhodium crucible	AIR	Melted at 1000 °C/1hr. Poured into 400 °C stainless steel mold, annealed at 370 °C. Cooled to rm temp at 1 °C/min.
SM2-30/30/40	30ZnO−30Bi$_2$O$_3$−40B$_2$O$_3$	125 g/platinum rhodium crucible	AIR	Melted at 1000 °C/1hr. Poured into 370 °C stainless steel mold, annealed at 370 °C. Cooled to rm temp at 1 °C/min.
SM3-30/40/30	30ZnO−40Bi$_2$O$_3$−30B$_2$O$_3$	150 g/platinum rhodium crucible	AIR	Melted at 1000 °C/1hr. Annealed at 370 °C. Cooled to rm temp at 1 °C/min.
SM4-40/30/30	40ZnO−30Bi$_2$O$_3$−30B$_2$O$_3$	170 g/platinum rhodium crucible	AIR	Melted at 1000 °C/1hr. Poured into 400 °C stainless steel mold, annealed at 370 °C. Cooled to rm temp at 3 °C/min.
SM5-32/32/32 + Li	31.66ZnO-31.66Bi$_2$O$_3$-31.67B$_2$O$_3$−5LiNO$_3$	150 g/platinum rhodium crucible	AIR	Melted at 1000 °C/1hr. Annealed at 330 °C. Cooled to rm temp at 1 °C/min.
SM6-32/32/32 + As	31.6ZnO-31.6Bi$_2$O$_3$-31.6B$_2$O$_3$-5.2As$_2$O$_3$	170 g/platinum rhodium crucible	AIR	Melted at 1000 °C/1hr. Annealed at 330 °C. Cooled to rm temp at 1 °C/min.

treatment temperatures ranged from 400 °C to 600 °C with durations up to 24 h. These temperatures and durations were chosen based on predicted nucleation and crystal growth temperatures determined by the location of DSC exothermic peaks [1,3]. Bulk samples were removed and cooled at room temperature.

2.5. Laser exposures

Laser writing of the glass was performed using an Amplitude Satsuma femtosecond (fs) laser system emitting pulses with a pulse duration of 350 fs, a pulse repetition rate of 500 kHz, with a wavelength of 1030 nm [12,13]. The sample was secured to a computer-controlled 3D-stage (Aerotech ALS130) that was translated at a speed of 0.1 mm s^{-1}, 0.5 mm s^{-1}, or 1 mm s^{-1} in the x-, y-, and z-axes relative to the laser beam to define the pattern. Laser patterning, which consisted of lines or two dimensional pads from multiple parallel lines, was conducted in the sample over areas of 1 mm × 1 mm and 100 μm in depth. The laser was focused using a 20x/0.4 NA objective. Powers ranged from 32 mW to 367 mW and were chosen to be below the observed ablation threshold.

3. Results and discussion

### 3.1. Base properties of glass melts

3.1.1. Glass melts

Glasses were chosen based on their positions inside the glass forming region of ZnO−Bi$_2$O$_3$−B$_2$O$_3$ as indicated in Fig. 1a [14]. All glasses appeared transparent and homogenously mixed upon cooling. The large melts (LM series) are shown in Fig. 1b and are indicated by the green dot in Fig. 1a. The small melts (SM series) are shown in Fig. 1b and are indicated by the orange, red, and blue dots in Fig. 1a. XRF and EDS measurements showed that the produced glasses were stoichiometrically similar to their targeted composition (batched mol%). EDS measurements for LM1-40/30/30 and LM2-40/30/30 can be found in Table 1. XRF measurements for LM1-40/30/30, LM2-40/30/30 and LM3-40/30/30 + As were found to similar within ±0.5 weight % (wt%) with their reference wt% calculated from batched mol%.

3.1.2. Thermal properties

The large melt compositions LM1-40/30/30 and LM2-40/30/30 both have similar glass transition temperatures (T_g) and glass crystallization temperatures (T_x) (Table 1, Fig. 2), suggesting that the melt protocol employed yielded repeatable glass with a common thermal history. The addition of As$_2$O$_3$ into the composition (LM3-40/30/30 + As) did not have any significant effect on the T_g or T_x. For the small melt of the same composition (SM3-40/30/30), both T_g and T_x decrease. For the small melts, changing the composition from 40/30/30 to 33/33/33 did not significantly change the T_g or T_x. It is important to note that the thermal history and cooling rate of the small melts are different from that of the larger melts, which could also be a factor in determining T_g or T_x. The addition of LiNO$_3$ to the 33/33/33 composition decreased both the T_g and T_x and introduced an endotherm at 595.6 °C. The decrease in T_g and T_x is most likely due to the decrease in crosslink density, as observed when adding Li$_2$O in a similar 40/30/30 composition [15]. The addition of As$_2$O$_3$ to the 33/33/33 composition increased both the T_g and T_x and introduced an exotherm at 603.9 °C. Overall, higher boron wt% resulted in higher T_g and T_x and a higher bismuth wt% resulted in lower T_g and T_x. This is due to the glass network becoming less tightly packed as the Bi$_2$O$_3$ content is increased [16−18]. All compositions exhibited endothermic peaks for melting at approximately 650°C−700 °C (Fig. 2).

3.1.3. Optical properties

The index of refraction for all melts is within the range of 1.9805−2.0663 (Table 2). The index of refraction is slightly higher for additional Bi$_2$O$_3$ content (SM1-33/33/33 & SM3-30/40/30). This has been observed for ZnO−Bi$_2$O$_3$−B$_2$O$_3$ glasses with increased ZnO or Bi$_2$O$_3$ content and can be explained via cation polarizability [18,19]. In ZnO−Bi$_2$O$_3$−B$_2$O$_3$ glasses, the molar refraction, which is partially dependent on the index of refraction, was observed to increase with the cation polarizability (Bi^{3+}, Zn^{2+}, and B^{3+}) and electronic polarizability (O^{2-}) when ZnO and/or Bi$_2$O$_3$ was increased [18]. All melts showed transmission that ranged from approximately 400 nm to 2.88 μm, typical for ZnO−Bi$_2$O$_3$−B$_2$O$_3$ based glasses. All melts have optical band edges (measured using Tauc plots) that ranged from 395 nm to 412 nm (Table 2). The band
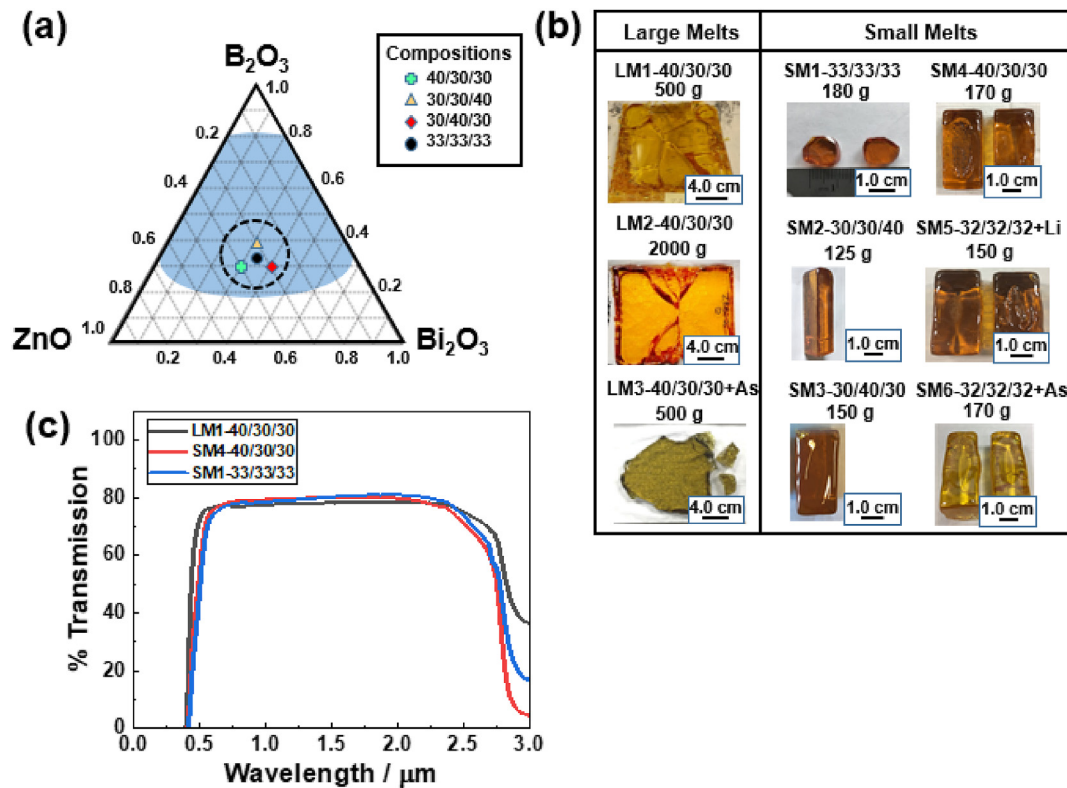
Fig. 1. (a) Ternary diagram of ZnO−Bi$_2$O$_3$−B$_2$O$_3$ glass system. The blue region is the glass forming region of ZnO−Bi$_2$O$_3$−B$_2$O$_3$ glass system. The colored symbols represent the compositions studied in this paper with green cross representing a ZnO−Bi$_2$O$_3$−B$_2$O$_3$ ratio of 40/30/30, orange triangle representing a ratio of 30/30/40, red diamond representing a ratio of 30/40/30, and black dot representing a ratio of 33/33/33. (b) Pictures of ZnO−Bi$_2$O$_3$−B$_2$O$_3$ glass compositions illustrating their respective melt sizes. Large melts range from 500 g to 2000g and small melts range from 180 g to 125 g. (c) Transmission measurements for samples LM1-40/30/30, SM1-33/33/33, and SM4-40/30/30. (For interpretation of the references to color in this figure legend, the reader is referred to the Web version of this article.)

edge shifts to lower wavelengths for glasses with increased ZnO over Bi$_2$O$_3$ content (Table 2). This may be due to the increase of density of state of Bi 6p orbitals [18]. Maximum percent transmission (%T) was similar for all glasses and ranged from 75.10% to 81.11% measured at 1 μm (Table 2). Changes in %T followed no noticeable trend. Transmission measurements are shown in Fig. 1c for samples LM1, SM1, and SM4. These samples were chosen as representative glasses from the large and small melts. LM1 and SM4 have the sample compositional ratios of 40/30/30 while SM1 has compositional ratios of 33/33/33. All show excellent transparency in the spectral range from approximately 400 nm to 2.88 μm. An example of base and post heat-treated UV−Vis transmission measurement for SM6-32/32/32 + As can be found in Section 2, Fig. 6.

3.1.4. Microstructure and molecular connectivity

XRD and Raman measurements confirmed that all glass compositions were amorphous after melt processing. Fig. 3 shows XRD and Raman measurements of as-melted LM1-40/30/30 glass. These findings were typical of all as-melted glass compositions. TEM and SAED measurements of the glasses showed that the glass compositions were phase separated. Fig. 3 shows the SAED and TEM images for LM1-40/30/30. The SAED patterns indicate that the base glass is amorphous, however, the TEM and EDS mapping shows that the glass is phase separated and that the size of the secondary phase, which is densely dispersed in the matrix, is approximately 5 nm. This was also observed for LM2-40/30/30. The brightness contrast indicates that the secondary phases consist of relatively heavier elements, in comparison with those in the matrix. The EDS mapping confirms that the secondary phase is Bi rich. Like Pb-oxide, Bi-oxide is readily reduced at elevated temperatures.

Although Bi has two oxidation states, only Bi^{3+} is found in glass, and so its reduction leads directly to metallic Bi. According to most reports on the melting of Bi-oxide containing glasses, it should be carried out in the presence of As$_2$O$_3$ and alkali metal nitrates to maintain the oxygen potential [18]. The LM3-40/30/30 + As base glass containing 0.5 wt% As$_2$O$_3$ with XRD and TEM was found to be amorphous, but still phase separated with ~2−3 nm particles, rich in Bi.

3.2. Crystallization behavior of glasses created in section 3.1

3.2.1. Initial heat treatments of glasses

Furnace-based heat treatment (HT) of glasses were performed according to the individual glass' nucleation temperatures, crystallization growth temperatures, and complete crystallization temperatures as determined by the location of DSC peaks. Initially, samples were HT'ed in an oven at 500 °C for 6 h per Zeng et al. [1]. At temperatures above 500 °C, SM1-33/33/33, SM3-30/40/30, SM4-40/30/30, and SM5-32/32/32 + Li glasses show signs of extensive surface crystallization and deformation with loss of optical transmission. LM1-40/30/30, LM2-40/30/30, LM3-40/30/30 + As, SM2-30/30/40, and SM6-32/32/32 + As glasses show that moderate surface crystallization can be removed via post-HT polishing (Fig. 4).

3.2.2. Surface crystallization

XRD and Raman analysis show that this surface crystallization was composed of the phases ZnO, BiB$_3$O$_6$, and Bi$_2$ZnB$_2$O$_7$ (Fig. 5a and b) [3,20]. Large ZnO surface crystals and nanorods were observed optically and through SEM imaging (Fig. 5). The
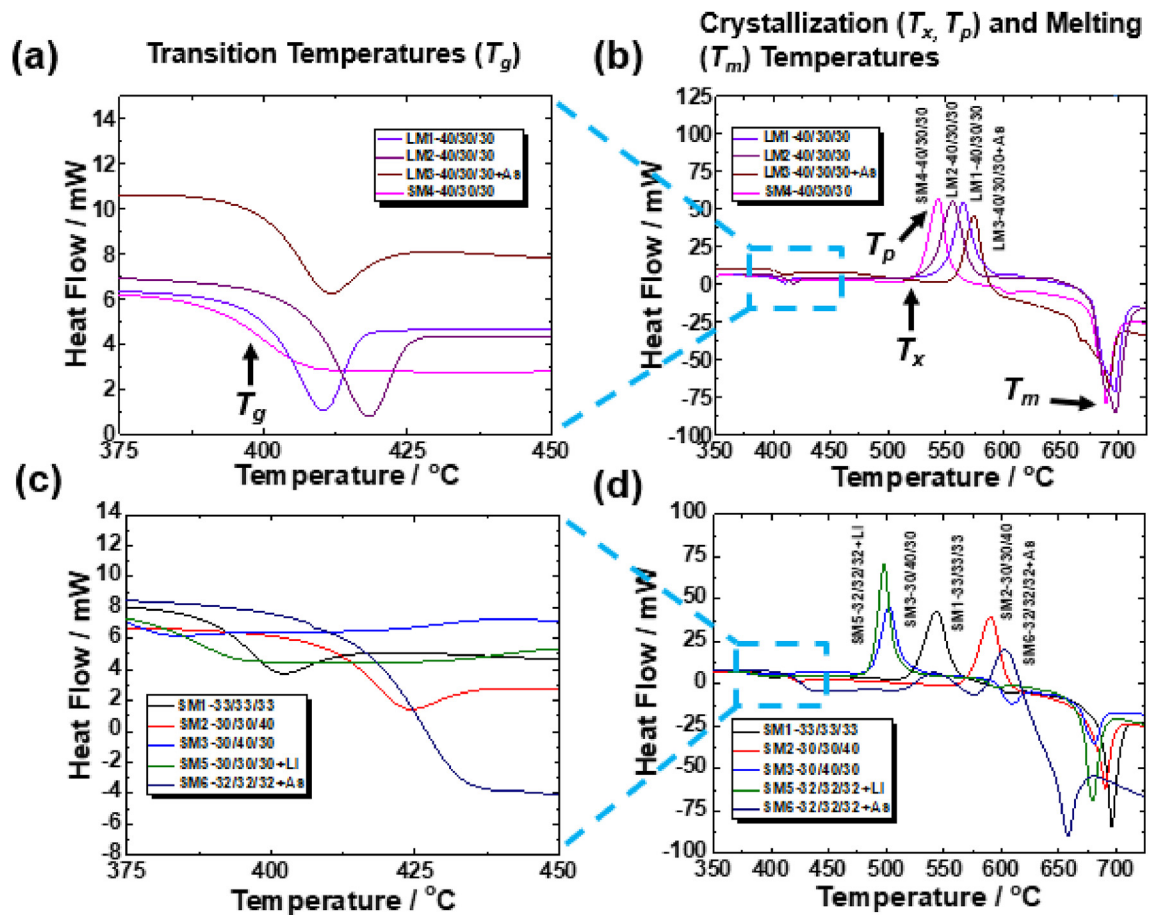
Fig. 2. DSC measurements of all melt compositions. Positive peaks are exothermic peaks and negative peaks are endothermic peaks on the y-axis. Transition temperatures, T_g (a) crystallization temperatures, T_x, T_p and melting temperatures, T_m (b) for LM1, LM2, LM3, and SM4 are shown together. Transition temperatures (c) crystallization and melting temperatures (d) for SM1, SM2, SM3, SM5, and SM6 are shown together. Each sample was powdered before measurement. The large peaks from 475 °C to 650 °C show the relative temperatures at which crystallization occurs for each glass. The inset shows a closer view of the T_g that occurs below 450 °C. T_g, T_x, T_p and T_m are indicated in (a) and (b) for SM4 as an example.

Table 2
Base properties (T_g, T_p, T_m, n) of $ZnO-Bi_2O_3-B_2O_3$ based glasses.

| Glass Sample	Glass Transition Temperature (T_g) Powder (°C)	Glass Crystallization Temperature (T_p) Powder (°C)	Endotherms Powder (°C)	Glass Melting Temperature (T_m) Powder (°C)	Index of Refraction (n) (±0.0005)	Max %T at 1.0 μm	Optical Band Edge
LM1-40/30/30	406.1	565.5		697.7	1.9977	77.45	395
LM2-40/30/30	406.6	553.9		697.4	1.9926	78.75	390
LM3-40/30/ 30 + As	407.6	560.0		694.5	1.9932	81.11	393
SM1-33/33/33	391.6	543.70		696.5	2.0173	79.39	412
SM2-30/30/40	408.42	590.78		691.2	1.9736	80.08	402
SM3-30/40/30	365.3	502.6	608.8	680.7	2.0663	80.83	411
SM4-40/30/30	388.5	543.7	606.3	689.1	1.9994	80.02	400
SM5-32/32/ 32 + Li	375.5	498.0	595.6	679.1	2.0051	75.10	388
SM6-32/32/ 32 + As	413.8	541.9, 603.9		658.1	1.9805	75.40	403

emergence of these phases and surface crystallization severely hinder or altogether prevents post-HT transmission. As the material cooled, the surface was observed to crystallize. Surface crystallization was also present in the cases of HTs using inert atmosphere.

SM1-33/33/33, SM3-30/40/30, SM4-40/30/30, and SM5-32/32/ 32 + Li all show complete volume crystallization and deformation post-HT, which rendered the sample opaque (Fig. 4). This is

indicative of all three phases being present throughout the surface and the bulk of the sample. In these cases, the surface crystallization could not be polished off. SM2-30/30/40 is partly transparent post-HT with only a thin layer of surface crystallization, however; no bulk $Bi_2ZnB_2O_7$ crystallization was observed via XRD. SM6-32/ 32/32 + As is partly transparent post-HT with only a thin layer of surface crystallization. In LM1-40/30/30 and LM2-40/30/30, after the surface crystallization was polished off, XRD confirmed the
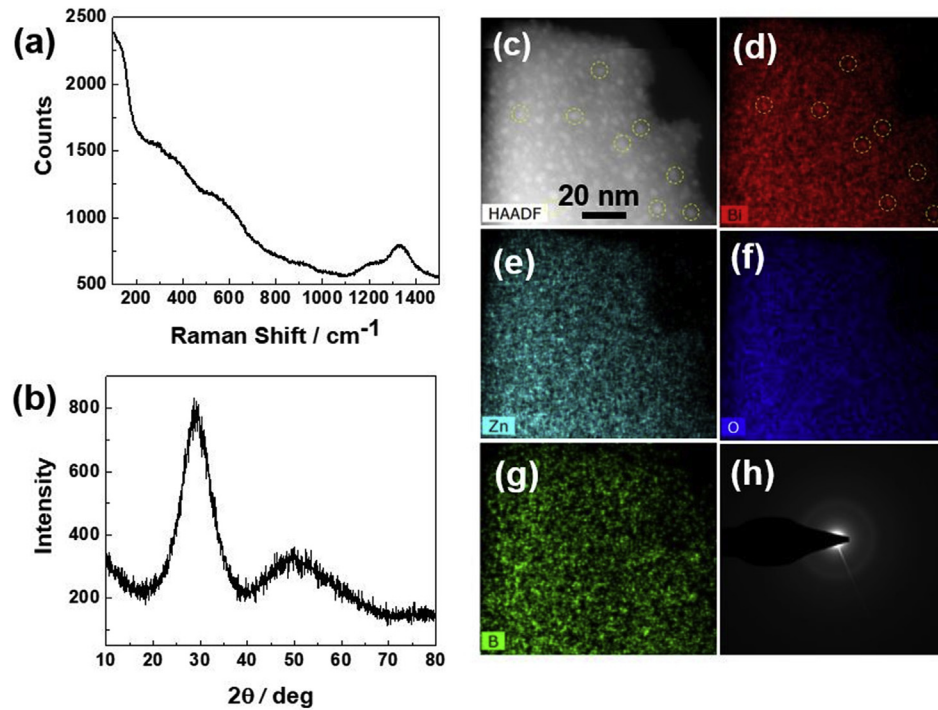
Fig. 3. (a) Raman and (b) XRD measurements of as-melted polished LM1-40/30/30 glass. TEM (c−g) and SAED (h) of the LM1-40/30/30 glass showed that the amorphous base glasses were phase separated with the secondary phase being Bi rich. The yellow circles seen in (c) and (d) show the distribution of Bi and that of the bright secondary phase, indicating there is a match. (For interpretation of the references to color in this figure legend, the reader is referred to the Web version of this article.)
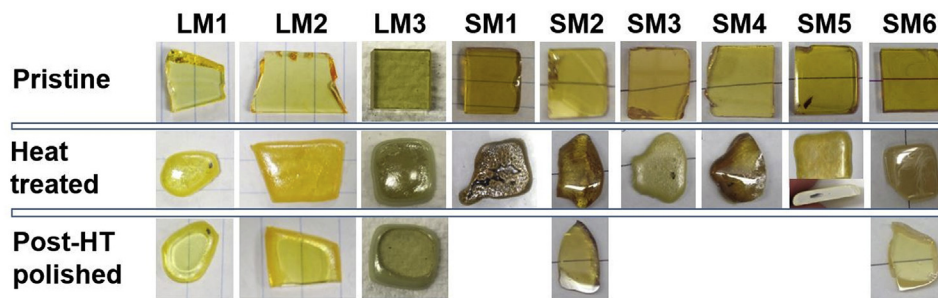
Fig. 4. Images of polished as-melted and post-HT (500 °C for 6 h) samples from each composition. If a sample image is not present for "post-HT polished" that indicates the sample was not able to be polished as it was completely opaque.

presence of bulk $Bi_2ZnB_2O_7$ crystal formation but only a minimal amount. In LM3-40/30/30 + As and SM6-32/32/32 + As, after the surface crystallization was polished off, XRD confirmed the presence of bulk $Bi_2ZnB_2O_7$ crystal formation. It is important to note that even when samples SM1-33/33/33, SM3-30/40/30, SM4-40/30/30, and SM5-32/32/32 + Li were HT'ed at lower temperatures, there was no significant presence of bulk $Bi_2ZnB_2O_7$ crystal formation.

Three courses of action were used to facilitate the growth of targeted $Bi_2ZnB_2O_7$ crystals in the amorphous $ZnO-Bi_2O_3-B_2O_3$ matrix with the goal of mitigating surface crystallization. The first was to further focus our next steps on the compositions that would lead to increased $Bi_2ZnB_2O_7$ crystal growth. The compositions chosen were LM3-40/30/30 + As and SM6-32/32/32 + As glasses which demonstrated less surface crystallization and maintained bulk crystallization of the $Bi_2ZnB_2O_7$ phase with transmission after polishing. The second course of action was to use multi-step nucleation-growth HT procedure as compared to the previously

used single step HT. The third was to use direct laser writing technique to expose only the bulk $ZnO-Bi_2O_3-B_2O_3$ matrix beneath the surface to initiate radiation-induced nucleation and/or growth and possibly avoid surface reactions that were shown to lead to surface crystallization. The outcome of these strategies is discussed.

3.2.3. Crystallization properties of LM3-40/30/30 + As & SM6-32/32/32 + As

Volume crystallization, which included the phases ZnO, BiB_3O_6, and $Bi_2ZnB_2O_7$, were identified and correlation with HT protocol for LM3-40/30/30 + As & SM6-32/32/32 + As glasses with post-HT transmission after surface polishing to remove crystallization. At lower temperature HTs (430 °C) the BiB_3O_6 phase dominated the amorphous bulk matrix while at higher HTs (450 °C−550 °C) and using multi-step nucleation and growth HTs, the desired $Bi_2ZnB_2O_7$ phase emerges and the BiB_3O_6 disappears [8]. No volume ZnO crystallization was found. This was consistent with findings from
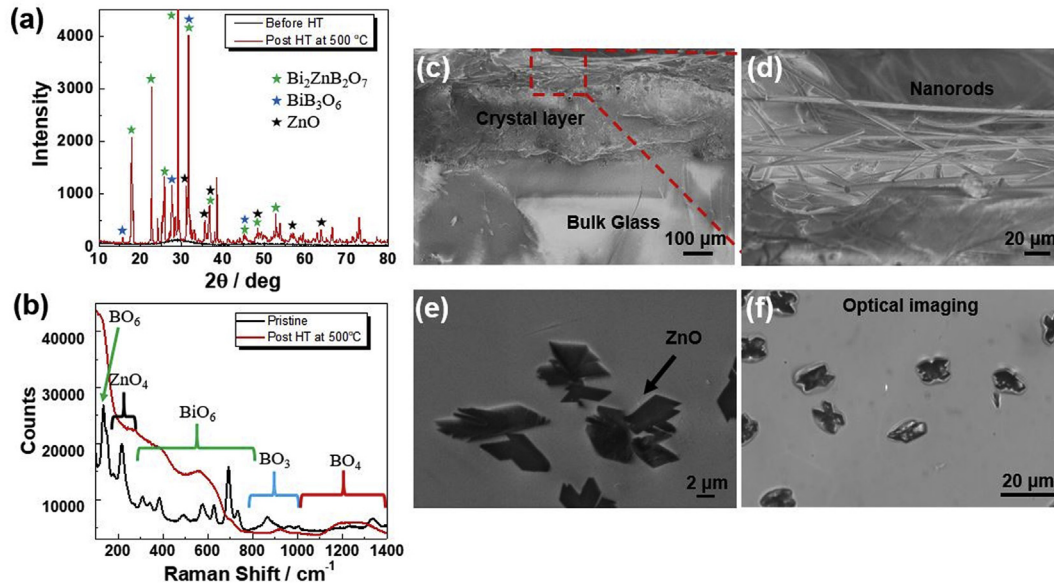
Fig. 5. (a) XRD and (b) Raman measurements of glass before and after heat treatment at 500 °C for 6 h. Both indicate the presence of the three phases ZnO, BiB_3O_6, and $Bi_2ZnB_2O_7$. (c) Profile SEM image of a heat treated glass with surface crystallization and an (d) expanded view of the surface nanorods. (e) SEM image and (f) optical image of the surface of a heat treated glass, showing ZnO.

Shanmugavelu et al. [3]. In his work studying $ZnO-Bi_2O_3-B_2O_3$ glasses, the Avrami exponent *n* value found suggested that both BiB_3O_6 and $Bi_2ZnB_2O_7$ first crystallize at the surface and then penetrate into the volume with increasing temperatures [2,3]. The Avrami exponent *n* value also indicates that the crystallization mechanism for $Bi_2ZnB_2O_7$ corresponds to three-dimensional growth [2]. The HTs which led to the greatest $Bi_2ZnB_2O_7$ phase growth in the amorphous bulk matrix are shown in Fig. 6.

XRD measurements show that the as-melted LM3-40/30/30 + As glass sample has an amorphous profile whereas the 500 °C HT'ed sample displays peaks consistent with $Bi_2ZnB_2O_7$ crystal formation (Fig. 6a). The two-step 430 °C for 24 h followed by 500 °C for 6 h HT'ed sample displays peaks consisted with $Bi_2ZnB_2O_7$ crystal formation with increased intensity. UV−Vis transmission

measurements for the LM3-40/30/30 + As glass shows a decrease in maximum transmission with a minimum edge shift for both HTs. This indicates that the LM3-40/30/30 + As glass sample has bulk crystal growth without transmission loss.

SAED patterns show that the base LM3-40/30/30 + As glass is amorphous (Fig. 6c,f). Bright field TEM images show that the base glass is phase separated. The secondary phase is densely dispersed in the matrix, ~2.9 nm, and based on brightness contrast, this is consistent with a heavier element composition compared to the matrix. For the 500 °C HT glass, SAED patterns show crystalline spots (Fig. 6d,g). Dark field TEM images show heavy particles with reduced sizes of ~2.0 nm are uniformly dispersed throughout the matrix. For the two-step HT'ed glass, SAED patterns show crystalline spots. Values extracted from the SAED patterns were
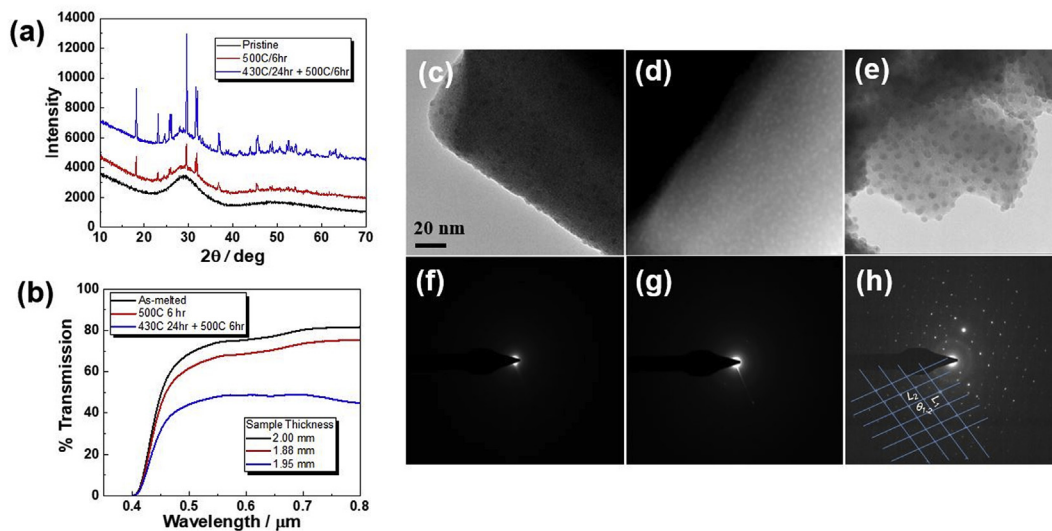
Fig. 6. (a) XRD patterns and (b) UV−Vis transmission measurements of LM3-40/30/30 + As amorphous as-melted glass, HT'ed at 500 °C for 6 h, and using the two step procedure 430 °C for 24 h followed by 500 °C for 6 h. TEM and SAED measurements of (c,f) amorphous as-melted LM3-40/30/30 + As glass, (d,g) HT'ed at 500 °C for 6 h, and (e,h) using the two step procedure 430 °C for 24 h followed by 500 °C for 6 h.
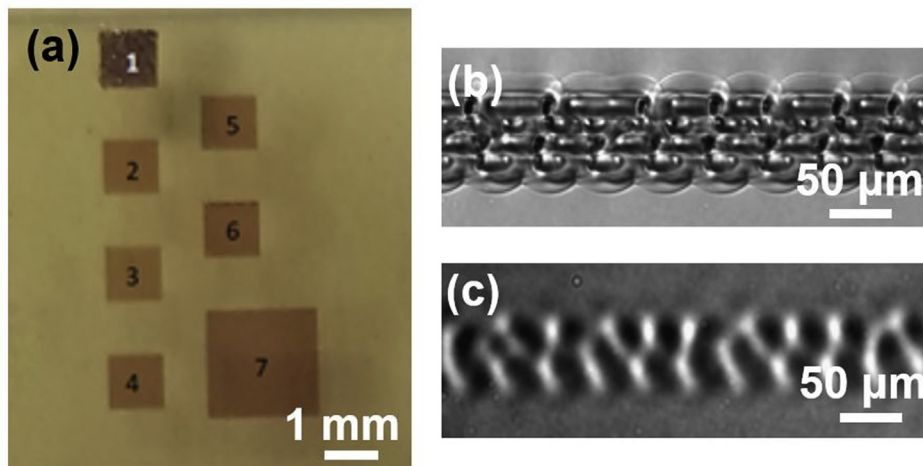
Fig. 7. (a) Top-down optical image of laser exposure pads in LM3-40/30/30 + As glass. (b) Top-down SEM image of laser exposed lines in LM3-40/30/30 + As glass. (c) Top-down SEM image of laser exposed lines in LM3-40/30/30 + As glass after being HT at 500 °C for 3 h and polished.

$L_1 = 2.7954$ Å, $L_2 = 2.4513$ Å, and $\theta_{1\text{-}2} = 103.070°$. This agrees with the literature values for $Bi_2ZnB_2O_7$ where $d_{(311)} = 2.8085$ Å (0.47% error with L1), $d_{(002)} = 2.4447$ Å (0.27% error with L_2) and $\theta_{(311)\text{-}(002)} = 103.391°$ (0.31% error with $\theta_{1\text{-}2}$) [21]. The precise match between the values extracted from bright crystalline spots in the SAED pattern and the values reported for $Bi_2ZnB_2O_7$ suggests that the major crystalline phase in the HT glass is $Bi_2ZnB_2O_7$. Dark field TEM images show heavy particles with increased sizes of ~5.0 nm uniformly dispersed throughout the matrix. For all HTs and volume crystallization the change in index of refraction was negligible and mostly attributed to relaxation of the glass.

3.2.4. Laser-induced crystallization

The following laser patterning parameters were used to fabricate the two dimensional pads seen in Fig. 7a. Pads 1 and 2 were laser scanned at speeds of 0.1 mm s^{-1}, pads 3, 4, 5 and 7 were scanned at speeds of 0.5 mm s^{-1}, and pad 6 was scanned at a speed of 1.0 mm s^{-1}. Pads 1−7 were laser exposed at powers of 367 mW, 199 mW, 240 mW, 199 mW, 171 mW, 199 mW, and 32 mW respectively. The laser was focused at 100 μm beneath the surface to avoid any surface related crystallization. These pads were prepared to assess the possibility of direct writing regions to either nucleate or grow, desired crystalline phases. Refractive index measurements were conducted on the base glass as well as post-exposed pads 3, 4, 6, and 7 quantifying index at a wavelength of 1880 nm. The refractive index measurements were then repeated for some pads after polishing to determine if any surface effects (crystallization, surface layer) could be observed that might have altered the measured index. Post-exposure transmission and absorbance was also measured for each pad. The lines patterned in Fig. 7b and c were fabricated at a power of 313 mW. This line sample was then HT'ed at 500 °C for 3 h, polished and SEM imaged.

Laser modification in the form of ablation was visible via SEM imaging of the LM3-40/30/30 + As sample surfaces for Pad 1 in Fig. 7a. Transmission was largely maintained for each laser exposed pad that was not ablated (Pads 2−7). An absorption peak was found at 530 nm for each laser exposed pad. This peak is most likely due to increased Bi content [22]. There was no significant Δn for any of the measured pads. It should also be noted that the patterned areas are very small which made accurate Δn measurement difficult to determine. The laser patterned lines seen in Fig. 7b have less visible index contrast post-HT. This indicates the possibility to control crystallization size, density, and depth via a combination of HTs and laser exposures.

4. Conclusions

The goal of this work was to create a $ZnO-Bi_2O_3-B_2O_3$ composition which would promote formation of $Bi_2ZnB_2O_7$ crystallites within the volume of the glass, upon heat treatments. We have first demonstrated control over glass transition temperature, T_g and crystallization temperature, T_x, index of refraction, n, of $ZnO-Bi_2O_3-B_2O_3$ glasses by varying composition/melting protocols. As-melted $ZnO-Bi_2O_3-B_2O_3$ based glasses were found to be amorphous, homogenous, and maintained base properties with scale up.

Heat treatments were conducted on $ZnO-Bi_2O_3-B_2O_3$ based glasses. Surface crystallization, containing the phases ZnO, BiB_3O_6, and $Bi_2ZnB_2O_7$ was observed for all glasses but was reduced for glasses containing As_2O_3. Better control over crystallization and targeted $Bi_2ZnB_2O_7$ phase content was demonstrated via heat treatment and laser exposures in $ZnO-Bi_2O_3-B_2O_3 + As_2O_3$ glasses. It is suggested that the crystallization mechanism starts at the surface along with all possible phases (ZnO, BiB_2O_6, $Bi_2ZnB_2O_7$) then extends into the bulk with increasing heat treatment temperature. The increase in $Bi_2ZnB_2O_7$ bulk crystallization with temperature is maximized for compositions with added As_2O_3. Control over crystallization size, density, and depth were obtained through laser exposures and heat treatments. Unfortunately, we were not able to achieve crystal-free glasses initially, even after a rapid initial quench, to provide a quantitative reference point for subsequent heat treatment studies. However, we believe this provides a stepping stone to the creation of optical devices with tunable properties and applications.

Declaration of competing interest

The authors declare that they have no known competing financial interests or personal relationships that could have appeared to influence the work reported in this paper.

Acknowledgments

References

[1] H. Zeng, Z. Liu, Q. Jiang, B. Li, C. Yang, Z. Shang, J. Ren, G. Chen, Large third-order optical nonlinearity of ZnO-Bi$_2$O$_3$-B$_2$O$_3$ glass-ceramic containing Bi$_2$ZnB$_2$O$_7$ nanocrystals, J. Eur. Ceram. Soc. 34 (2014) 4383−4388, https://doi.org/10.1016/j.jeurceramsoc.2014.06.031.

[2] Z. Liu, H. Zeng, X. Ji, J. Ren, G. Chen, J. Ye, Y. Dai, Y. Cheng, Formation of Bi$_2$ZnB$_2$O$_7$ nanocrystals in ZnO-Bi$_2$O$_3$-B$_2$O$_3$ glass induced by femtosecond laser, J. Am. Ceram. Soc. 98 (2015) 408−412, https://doi.org/10.1111/jace.13330.

[3] B. Shanmugalevu, V.V. Ravi Kanth Kumar, Crystallization kinetics and phase transformation of bismuth zinc borate glass, J. Am. Ceram. Soc. 95 (2012) 2891−2898, https://doi.org/10.1111/j.1551-2916.2012.05342.x.

[4] T. Honma, Y. Benino, T. Fujiwara, R. Sata, T. Komatsu, New optical nonlinear crystallized glasses and YAG laser-induced crystalline dot formation in rare-earth bismuth borate system, Opt. Mater. 20 (2002) 27−33, https://doi.org/10.1016/S0925-3467(02)00027-7.

[5] H. Oo, H. Mohamed-Kamari, W. Wan-Yusoff, Optical properties of bismuth tellurite based glass, Int. J. Mol. Sci. 13 (2012) 4623−4631, https://doi.org/10.3390/ijms13044623.

[6] H. Hellwig, J. Liebertz, L. Bohaty, Linear optical properties of the monoclinic bismuth borate BiB$_3$O$_6$, J. Appl. Phys. 88 (2000) 240−244, https://doi.org/10.1063/1.373647.

[7] L. Li, G. Li, Y. Wang, F. Liao, J. Lin, Bismuth Borates: two new polymorphs of BiB$_3$O$_6$, Inorg. Chem. 44 (2005) 8243−8248, https://doi.org/10.1021/ic050190k.

[8] C. Schwarz, M. Kang, C. Pantano, K. Richardson, C. Rivero-Baleine, S. Kuebler, C. Grabill, J. Rice, Q. Altemose, K. Richardson, B. Schnable, I. Wietecha-Reiman, E. Haldeman, Optical and crystal growth studies of ZnO-Bi$_2$O$_3$-B$_2$O$_3$ glass in Proc. SPIE, advanced optics for defense applications: UV through LWIR III, 2018, p. 10627, https://doi.org/10.1117/12.2304446.

[9] Q. Altemose, K. Raichle, B. Schnable, C. Schwarz, M. Kang, C. Pantano, K. Richardson, C. Rivero-Baleine, In situ X-ray diffraction studies of crystallization growth behavior in ZnO-Bi$_2$O$_3$-B$_2$O$_3$ glass as a route to functional optical devices, MRS Adv. 3 (2018) 563−567, https://doi.org/10.1557/adv.2017.640.

[10] T. Inoue, X. Gao, K. Shinozaki, T. Honma, T. Komatsu, Laser patterning of non-linear optical Bi$_2$ZnB$_2$O$_7$ crystal lines in glass, Front. Mater. 2 (2015) 1−7.

[11] A. Bajaj, A. Khanna, B. Chen, J.G. Longstaffe, U.-W. Zwanziger, J.W. Zwanziger, Y. Gomez, F. Gonzalez, Structural investigation of bismuth borate glasses and crystalline phases, J. Non-Cryst. Solids 355 (2009) 45−53, https://doi.org/10.3389/fmats.2015.00042.

[12] I. Mingareev, T. Bonhoff, A.F. El-Sherif, W. Meiners, I. Kelbassa, T. Biermann, M. Richardson, Femtosecond laser post-processing of metal parts produced by laser additive manufacturing, J. Laser Appl. 25 (2013) 052009, https://doi.org/10.2351/1.4824146.

[13] J. Choi, M. Ramme, T. Anderson, M.C. Richardson, Femtosecond laser written embedded diffractive optical elements and their applications in Proc. SPIE 7589, Front. Ultrafast Opt.: Biomed. Sci. Ind. Appl. X (2010) 75891A, https://doi.org/10.1117/12.843697.

[14] N.M. Bobkova, E.E. Trusova, Low-melting bismuth−borate glass: composition development, Glass Ceram. 68 (2012) 349−352, https://doi.org/10.1007/s10717-012-9387-3.

[15] S. Bale, S. Rahman, Spectroscopic and physical properties of Bi$_2$O$_3$-B$_2$O$_3$-ZnO-Li$_2$O glasses, ISRN Spectrosc. (2012) 1−7, https://doi.org/10.5402/2012/634571.

[16] D. Saritha, Y. Markandeya, M. Salagram, M. Vithal, A.K. Singh, G. Bhikshamaiah, Effect of Bi$_2$O$_3$ on physical, optical and structural studies of ZnO−Bi$_2$O$_3$−B$_2$O$_3$ glasses, J. Non-Cryst. Solids 354 (2008) 5573−5579, https://doi.org/10.1016/j.jnoncrysol.2008.09.017.

[17] X. Zhu, C. Mai, M. Li, Effects of B$_2$O$_3$ content variation on the Bi ions in Bi$_2$O$_3$−B$_2$O$_3$−SiO$_2$ glass structure, J. Non-Cryst. Solids 388 (2014) 55−61, https://doi.org/10.1016/j.jnoncrysol.2013.12.007.

[18] T. Hashimoto, Y. Shimoda, H. Nasu, A. Ishihara, ZnO−Bi$_2$O$_3$−B$_2$O$_3$ glasses as molding glasses with high refractive indices and low coloration codes, J. Am. Ceram. Soc. 94 (2011) 2061−2066, https://doi.org/10.1111/j.1551-2916.2010.04383.x.

[19] S. Kumari, D. Mohan, S. Yadav, Effect of Bi$_2$O$_3$ content on non linear optical properties of TeO$_2$.Bi$_2$O$_3$.B$_2$O$_3$.ZnO glass system in Proc. of the national conference on recent advances in condensed matter physics, RACMP AIP Conf. Proc. 2093 (2019) 020049, https://doi.org/10.1063/1.5097118.

[20] F. He, Z. He, J. Xie, Y. Li, IR and Raman spectra properties of Bi$_2$O$_3$-ZnO-B$_2$O$_3$-BaO quaternary glass system, Am. J. Anal. Chem. 5 (2014) 1142−1150, https://doi.org/10.4236/ajac.2014.516121.

[21] J. Barbier, N. Penin, L.M. Cranswick, Melilite-type borates Bi$_2$ZnB$_2$O$_7$ and CaBiGaB$_2$O$_7$, Chem. Mater. 17 (2005) 3130−3136, https://doi.org/10.1021/cm0503073.

[22] Y. Fujimoto, M. Nakatsuka, Infrared luminescence from bismuth-doped silica glass, Jpn. J. Appl. Phys. 40 (2001) L279−L281, https://doi.org/10.1143/JJAP.40.L279.